Published in final edited form as:
NeuroImage. 2015 Jul; 114:136-146. DOI: 10.1016/j.neuroimage.2015.03.068

Orientation Dependence of Magnetization Transfer Parameters in Human White Matter

André Pampel[a,1,*], Dirk K. Müller [a,1,2], Alfred Anwander [a], Henrik Marschner [a], Harald E. Möller [a]

[a] Max Planck Institute for Human Cognitive and Brain Sciences, Leipzig, Germany.

[1] Joint first authors.

[2] Current address: Department of Psychiatry and Neuroimaging Center, Technical University Dresden, Dresden Germany

* Address for correspondence:

André Pampel

Max Planck Institute for Human Cognitive and Brain Sciences

Stephanstrasse 1a, 04103 Leipzig, Germany.

http://www.cbs.mpg.de/~pampel

phone: +49 341 9940 2233

Abstract

Quantification of magnetization-transfer (MT) experiments is typically based on a model comprising a liquid pool “a” of free water and a semisolid pool “b” of motionally restricted macromolecules or membrane compounds. By a comprehensive fitting approach, high quality MT parameter maps of the human brain are obtained. In particular, a distinct correlation between the diffusion-tensor orientation with respect to the $\mathbf{B}_0$-magnetic field and the apparent transverse relaxation time, T_2^b, of the semisolid pool (i.e., the width of its absorption line) is observed. This orientation dependence is quantitatively explained by a refined dipolar lineshape for pool b that explicitly considers the specific geometrical arrangement of lipid bilayers wrapped around a cylindrical axon. The model inherently reduces the myelin membrane to its lipid constituents, which is motivated by previous studies on efficient interaction sites (e.g., cholesterol or galactocerebrosides) in the myelin membrane and on the origin of ultrashort T_2 signals in cerebral white matter. The agreement between MT orientation effects and corresponding forward simulations using empirical diffusion imaging results as input as well as results from fits employing the novel lineshape support previous suggestions that the fiber orientation distribution in a voxel can be modelled as a scaled Bingham distribution.

Keywords

Absorption lineshape, anisotropy, Bingham distribution function, cerebral white matter, orientation dependence, fiber orientation distribution, quantitative magnetization-transfer imaging, super-Lorentzian lineshape

1. Introduction

The proton (^{1}H) spin relaxation of water in biological tissues is strongly affected by dipolar couplings to semisolid compounds, such as proteins or membrane components [1]. As a consequence, different tissue types have distinct relaxation times, which is widely exploited in magnetic resonance imaging (MRI) for generating contrast. Dipolar couplings are further utilized in magnetization-transfer (MT) experiments to obtain indirect information on the broad nuclear magnetic resonance (NMR) spectrum (order of tens of kHz) of the semisolid compounds. In the most common implementation, the semisolid spin system is saturated by radiofrequency (RF) irradiation off-resonance from the narrow water line [2, 3]. Via cross relaxation or chemical exchange, this pertubation is transferred to the water spin system leading to a transient signal change. In quantitative MT imaging (qMTI), the effect is typically studied as a function of the strength and frequency of the off-resonance irradiation to obtain so-called "Z-spectra" [4], to which a mathematical model is fitted (*e.g.*, the binary spin-bath or 'BSB' model [5]).

The cross-relaxation rate is determined by the type and number of binding sites for water on the semisolid components and the molecular dynamics of the system [1]. Of particular importance in nerve tissue is myelin, a lamellar membraneous structure enveloping axons [6]. Previous work demonstrated correlations between the relative size of the semisolid pool estimated by MT experiments and histological measures of myelin content (*e.g.*, [7]).

As dipole-dipole interactions depend on orientation (*i.e.*, the angle between the axis connecting the interacting dipoles and the direction of the main magnetic field, $\mathbf{B}_0$; we will, thus, use the term 'orientation' as a substitute of 'orientation with respect to $\mathbf{B}_0$' from here on), one might expect anisotropic MT in tissues exhibiting orientational anisotropy Consistently, orientation-dependent T_1 relaxation has been shown for water attached to membrane surfaces in model systems [8]. Moreover, variation of the signal intensity with orientation (so-called "magic angle effect") was demonstrated in T_1- and T_2-weighted MRI of peripheral nerve tissue [9]. For MT, however, Henkelman *et al.* [10] reported an inability to identify a corresponding orientational dependence in samples from corpus callosum and optic nerve and proposed that observation of MT anisotropy would require a tissue geometry composed of multiple parallel sheets, which does not seem to be provided in tissues on a macroscopic scale. Hence, MT has been assumed to be isotropic in brain tissue.

Inconsistent with this general assumption, we recently observed a correlation of BSB model parameters, in particular the transverse relaxation constant of the semisolid pool, T_2^b, and the orientation of major white-matter (WM) fiber bundles [11]. A similar T_2^b contrast variation with fiber tract directionality was subsequently also reported by Yarnykh [12] without providing an explanation of the underlying mechanism. We hypothesize that anisotropy as observed in these MT experiments is a general phenomenon that is caused by an orientation dependence of the RF absorption lineshape of the semisolid pool. Although the commonly used super-Lorentzian (SL) lineshape is per se isotropic, this is not the case for its underlying dipolar nature, and orientational invariance only results from 'powder averaging' over randomly oriented membrane segments [13]. Based on a more sophisticated tissue model, we demonstrate that a random distribution of membrane segment orientations is not a valid assumption for WM lipid membranes of fiber bundles. Consequently, apparent anisotropy of MT parameter maps can result from neglecting inherent orientation effects on the lineshape.

To investigate potential anisotropy empirically, MT and diffusion-weighted (DW) images were obtained from healthy human volunteers. Among the MT parameters, a special focus is on T_2^b as a function of the WM fiber orientation relative to $\mathbf{B}_0$. For a theoretical analysis, the SL lineshape is revisited, and a novel lineshape is derived for myelinated fiber bundles. Consequences of this lineshape are evaluated in two ways, by simulations with typical BSB parameters found in human WM and by fitting MT parameters to *in-vivo* data. With both approaches, the distinct orientation dependence of T_2^b obtained with standard fitting disappears, whereas the values of the other BSB parameters are reproduced.

2. Theory

2.1. Binary Spin-Bath Model for MT

In the BSB model, tissue is subdivided into two compartments, a liquid pool "a" (free water) and a semisolid pool "b" (motionally restricted molecules) [2, 4, 5, 14–17]. Both are considered to be in close contact allowing exchange of magnetization via chemical exchange or cross relaxation. These compartments are characterized by their equilibrium magnetizations, $M_0^{a,b}$, longitudinal and transverse relaxation rates, $R_1^{a,b} = 1/T_1^{a,b}$ and $R_2^{a,b} = 1/T_2^{a,b}$, respectively, and pseudo-first-order rate constants, $RM_0^{a,b}$, describing the transfer of longitudinal magnetization, $M_z^b \rightleftharpoons M_z^a$ [5]. The signal is proportional to σM_z^a, where all scanner-dependent effects are lumped into the scaling factor σ.

The time evolution of the magnetization is described by simplified Bloch-McConnel equations [18]. Subsequently, we will utilize an approach based on matrix algebra to solve them without unwarranted simplifications [17]. Because T_2^b is very short, transverse magnetization of the semisolid pool is not considered [19]. However, saturation of M_z^b due to off-resonance irradiation at frequency $\Omega = \omega_0 - \omega_{\mathrm{rf}}$ is described by an RF saturation rate [5]:

$$R_{\mathrm{rf}}^b = -\pi\omega_1^2 g^b(\Omega) \quad \text{with} \quad |\omega_1| = |\gamma B_1|\,, \tag{1}$$

where γ is the magnetogyric ratio, ω_0 is the Larmor frequency, and ω_{rf} and B_1 are the frequency and amplitude of the applied RF field, respectively. $g^b(\Omega)$ is the absorption lineshape for the semisolid pool. It depends on the associated transverse relaxation time, T_2^b, which is determined by the local microstructure.

A typical MT investigation involves preferable saturation of the semisolid pool and observation of a steady-state liquid-pool magnetization. As there is a distinct interdependence of some parameters, only six BSB parameters can be uniquely determined: σM_0^a, $M_0^b/(R_1^a M_0^a)$, RM_0^a, R_1^b, $1/(R_1^a T_2^a)$, and T_2^b (from R_{rf}^b) [5]. R_1^a can be extracted using a relaxation rate R_1^{obs} that may be obtained from an inversion-recovery experiment [5] or, alternatively, all above parameters plus R_1^a can be determined directly from MT data recorded with different excitation flip angles, α, and/or repetition times, T_R [17].

2.2. Super-Lorentzian Lineshape

An SL lineshape has been successfully employed for modeling MT in many tissues [14, 15]. It arises from partially ordered systems, notably lipid bilayers forming biological membranes [13, 20, 21]. Briefly, due to restricted molecular mobility, dipolar interactions in liquid-crystalline membranes are not completely averaged out but only reduced to some extent. For rapid molecular rotations or chain motions, the interactions are projected along the normal to the membrane, and the time-averaged dipolar Hamiltonian for an oriented membrane segment can be written as [13]:

$$\langle\hat{\mathcal{H}}_D(\theta_n)\rangle = \langle\hat{\mathcal{H}}_D(0)\rangle P_2\left(\cos\theta_n\right), \tag{2}$$

θ_n is the angle between the bilayer normal and $\mathbf{B}_0$, and $P_2(x) = (3x^2 - 1)/2$ is the second Legendre polynomial. Equation (2) predicts that the shape of the absorption line is unaffected by a change in the segment orientation while the frequency axis changes

according to $P_2(\cos\theta_n)$. The resulting lineshape for one segment is:

$$g^b(\Omega,\theta_n) = \frac{2}{|3\cos^2\theta_n - 1|}\; f\left(\frac{2\,\Omega}{|3\cos^2\theta_n - 1|}\right). \tag{3}$$

The function $f(\Omega,\theta_n)$ is not easily accessible, yet it is reasonable to assume a Gaussian [13, 20–22]:

$$f(\Omega,\theta_n) = \frac{1}{\sqrt{2\pi}\, r_2^b(\theta_n)} \exp\left\{-\frac{1}{2}\left[\frac{\Omega}{r_2^b(\theta_n)}\right]^2\right\}. \tag{4}$$

Scaling of the linewidth manifests itself in the orientation dependence of the width parameter $r_2^b(\theta_n)$:

$$r_2^b(\theta_n) = \frac{|3\cos^2\theta_n - 1|}{2\,T_2^b}. \tag{5}$$

In multilamellar systems with equally distributed segment orientations, a powder average has to be computed, from which the SL lineshape is derived:

$$g_{\mathrm{SL}}^b(\Omega) = \frac{1}{\sqrt{2\pi}} \int_0^{\pi/2} \frac{2\,T_2^b}{|3\cos^2\theta_n - 1|} \exp\left[-\frac{1}{2}\left(\frac{2\,\Omega\,T_2^b}{|3\cos^2\theta_n - 1|}\right)^2\right] \sin\theta_n d\theta_n. \tag{6}$$

It does not show any anisotropy but is a superposition of Gaussians, with a singularity that results from segments oriented at the magic angle ($\theta_n \approx 54.7°$) [13].

In the spectrum of a real sample, a singularity is not observed due to further (dipolar) interactions [13] and small variations of $\theta_n$within a segment ('mosaic spread') [23]. Experimentally, residual linewidths of 9-30 Hz have been found in lipid bilayers aligned at the magic angle [24–26]. A well-established procedure to account for such additional broadening is to convolve $g_{\mathrm{SL}}^b(\Omega)$ with an appropriate function [27]. Motivated by experimental findings [20, 22, 24–26], we choose a Gaussian as convolution kernel. As the convolution of two Gaussians is another Gaussian, this leads to

$$g_{\mathrm{SL}}^b(\Omega) = \frac{1}{\sqrt{2\pi}} \int_0^{\pi/2} \frac{1}{\sqrt{(R_2^{\mathrm{res}})^2 + r_2^b(\theta_n)^2}} \exp\left\{-\frac{1}{2}\frac{\Omega^2}{(R_2^{\mathrm{res}})^2 + r_2^b(\theta_n)^2}\right\} \sin\theta_n d\theta_n \tag{7}$$

with a total relaxation rate, R_2^{tot}, composed of $r_2^b(\theta_n)$ and an orientation-independent residual constant, R_2^{res}:

$$(R_2^{\mathrm{tot}})^2 = (R_2^{\mathrm{res}})^2 + (r_2^b(\theta_n))^2. \tag{8}$$

Henceforth, we assume $R_2^{\mathrm{res}} = 31.4\ \mathrm{s}^{-1}$ in all computations. This value results in a full width at half maximum of 11.7 Hz of the convolution kernel matching experimental findings [24–26]. In summary, the line-shape of a bilayer segment oriented at the magic angle is determined by R_2^{res} and much narrower than lines of segments oriented at other angles, which are determined by $r_2^b(\theta_n)$.

2.3. Absorption Lineshape for a Single Myelinated Fiber

The assumption of random segment orientations does not consider the specific coherence of orientations in a nerve fiber with lamellae of myelin enveloping an axon. As a more realistic model, we assume an idealized myelin sheath of cylindrical symmetry and restrict the analysis to segments on the lateral surface of the bilayers. For this configuration, θ_n will be a function of the axon orientation with respect to $\mathbf{B}_0$ (*i.e.*, its polar angle, θ, in the laboratory frame) and the azimuth, ϕ_A, in the axon frame (Fig. 1):

$$\cos\theta_n = -\sin\theta\cos\phi_A. \tag{9}$$

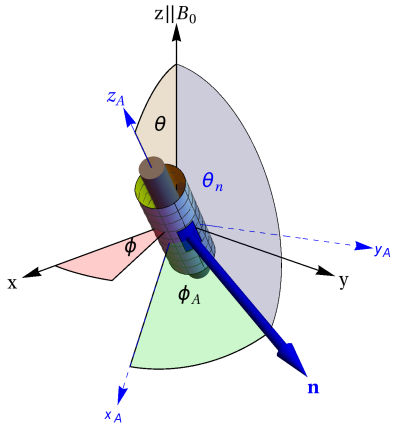

Figure 1: Spherical coordinates describing the orientation of a bilayer segment wrapped around a cylindrical axon. The polar angle of the membrane normal in the laboratory frame, xyz, is θ_n. Transformation into an axon frame, $x_A y_A z_A$, for which the z_A-axis is defined by the cylinder axis, is achieved by subsequent rotations about the y-axis by θ, and about the z-axis by ϕ. The azimuth of the membrane normal in the axon frame is ϕ_A. Note that θ_n does not depend on ϕ. An alternative animated version of this Figure is shown as Supplementary Figure S1.

Averaging over all segment orientations in the "cylinder model" (cyl) has to be performed for the full range of ϕ_A but with constant θ. Hence, after inserting Eq. (9) into Eqs. (3) and (4) and defining

$$r_2^b(\theta,\phi_A) = \frac{\left|3\cos^2\phi_A\sin^2\theta - 1\right|}{2\,T_2^b} \tag{10}$$

analogous to Eq. (5), a novel lineshape function is obtained:

$$g_{\mathrm{cyl}}^b(\Omega,\theta) = \frac{1}{(2\pi)^{3/2}}\int_0^{2\pi}\frac{1}{\sqrt{(R_2^{\mathrm{res}})^2 + (r_2^b(\theta,\phi_A))^2}} \times \exp\left[-\frac{1}{2}\frac{\Omega^2}{(R_2^{\mathrm{res}})^2 + (r_2^b(\theta,\phi_A))^2}\right] d\phi_A. \tag{11}$$

Evidently, Eq. (11) shows orientation dependence. For $\theta = 0°$, ϕ_A drops out of Eq. (10), and the lineshape for an ideal fiber aligned with $\mathbf{B}_0$ is a pure Gaussian. For $\sin\theta < 1/\sqrt{3}$ (*i.e.*, $\theta < 35.2644°$), r_2^b is nonzero regardless of ϕ_A. Hence, the sharp peak at $\Omega = 0$ that characterizes the SL lineshape does not form, and Eq. (11) yields a bell-shaped superposition of scaled Gaussians with decreasing width (and correspondingly increasing intensity) for increasing θ. This is shown in Fig. 2.

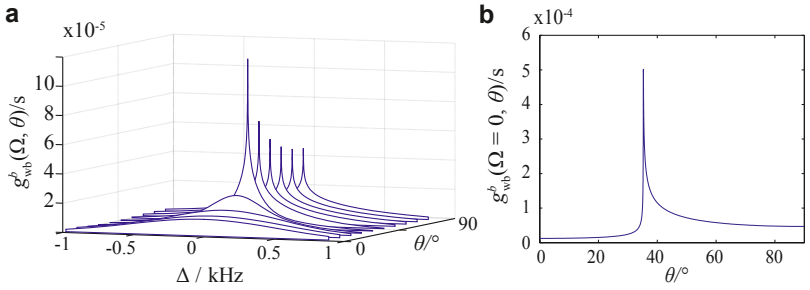

Figure 2: **(a)** Lineshape (highly exaggerated) for the wb model obtained with Eq. (11) and $R_2^{\mathrm{res}} = 31.4$ s^{-1}; $\Delta = \Omega/(2\pi)$. **(b)** Variation of the amplitude as a function of θ. Note the different scaling of the axes.

For $\sin\theta > 1/\sqrt{3}$, $r_2^b(\theta, \phi_A)$ has four roots in $\phi_A \in [0, 2\pi]$ leading to contributions from narrow and intense Gaussians characterized by R_2^{res}. Thus, integration over ϕ_A yields a lineshape similar to the SL (Fig. 2a). At $\sin\theta = 1/\sqrt{3}$, two roots are degenerate, and the maximum intensity is observed. For larger values of θ the intensity decreases accompanied by an apparent broadening of the line (Fig. 2b).

2.4. Absorption Lineshape for a Bundle of Myelinated Fibers

While one angle θ is sufficient to characterize the lineshape of a single axon, the situation is more complex on the macroscopic scale of a typical MRI voxel. The assumption of a distinct fiber population does not hold for the majority of WM voxels ('crossing fiber problem') [28], and even in regions with relatively coherent fiber bundles, such as the corpus callosum, axons are not perfectly parallel but demonstrate some degree of spreading or bending [29–31]. For adaptation of the lineshape model, we assume that individual fibers consist of cylindrical segments that can be described as wrapping bilayers and introduce a fiber orientation distribution function (fODF) to account for multidirectionality (including fiber crossings and spreading in each main direction).

The fODF represents the fraction of fibers oriented along a given direction and may be estimated, for example, by spherical deconvolution from DW-MRI data [32, 33]. To parameterize the peaks of the fODF and employ the result as measure for the spreading of the main fiber direction within a voxel, we follow previous suggestion [34, 35] to use

the antipodally symmetric Bingham probability distribution [36]. It is the analogue to the general bivariate normal distribution on the unit sphere. Recent results demonstrate that the scaled Bingham distribution can be fitted separately to each peak of the fODF to derive parameters for quantitative characterization of a fiber population [35]. A scaled Bingham distribution function is defined as [35]

$$\beta(\mathbf{u}) = f_0 \exp\left[-k_1 \left(\boldsymbol{\mu}_1 \cdot \mathbf{u}\right)^2 - k_2 \left(\boldsymbol{\mu}_2 \cdot \mathbf{u}\right)^2\right], \tag{12}$$

where $\mathbf{u}$ is a point on the unit sphere's surface, and f_0 is a scaling parameter. $k_1 \leq k_2$ are so-called concentration parameters along axes $\boldsymbol{\mu}_1$ and $\boldsymbol{\mu}_2$, respectively. These parameters characterize the width and ovality of the distribution (*i.e.*, the larger k_i the sharper the peak in the corresponding direction) as well as its orientation. The mean direction of the distribution is given by the vector $\boldsymbol{\mu}_0 = \boldsymbol{\mu}_1 \times \boldsymbol{\mu}_2$ and is used to identify the main fiber orientation of the fitted fODF peak. In spherical coordinates, $\mathbf{u}$ is a function of θ and ϕ (laboratory frame). By combining Eqs. (11) and (12), the lineshape function for myelinated fiber bundle(s) (fb) becomes

$$g^b_{\mathrm{fb}}(\Omega) = \mathcal{N} \int_0^{\pi} \int_0^{2\pi} g^b_{\mathrm{cyl}}(\Omega, \theta) \sum\nolimits_i \beta_i(\theta, \phi) \sin\theta \, d\theta d\phi, \tag{13}$$

where $\mathcal{N}$ is a normalization factor and the index $i \geq 1$ denotes the number of fODF peaks assumed to reflect different fiber bundles in the voxel.

3. Experimental Methods

3.1. Imaging Experiments

Seven healthy volunteers (4 female, mean age 26 y, range 19-33 y) were examined after obtaining informed written consent in accordance with ethically approved local policies. Brain MRI scans were recorded at 3 T with a MAGNETOM TIM Trio (Siemens, Erlangen, Germany) operated by *syngo* MR B 15 software. The body coil was used for RF transmission, and a 32-channel head array was used for signal reception.

An exhaustive description of the qMTI procedures has been published elsewhere [17]. Briefly, an MT-prepared gradient-recalled echo (GRE) sequence ($\alpha = 10°$; echo time, T_E = 6.7 ms; gradient and RF spoiling; 297 dummy cycles; 11 averages) was used to image a single axial slice (nominal voxel size 1.7 × 1.7 × 1.5 mm^3) at the level of the basal ganglia (slice position was shifted cranially in one case). To obtain sufficiently densely sampled Z-spectra, 32 scans were acquired with variation of offset frequency (0.2 kHz $\leq \Omega/2\pi \leq$ 50 kHz) and amplitude (1003 rad/s $\leq \omega_{1,max} \leq$ 5016 rad/s corresponding to

nominal flip angles of $180° \leq \alpha_{sat} \leq 900°$) of the Gaussian MT pulse (duration 10 ms; bandwidth 300 Hz) and with variation of T_R (33.6, 80, and 120 ms; 3 acquisitions with $T_R = 120$ ms not available in one case due to technical problems). B_0 and B_1 maps were recorded with GRE-based multiple-echo (8 echoes; 1.3 ms $\leq T_E \leq$ 20.1 ms) [37] and multiple-T_R (20 and 100 ms; $\alpha = 60°$) techniques [38], respectively.

Twice-refocused spin-echo echo-planar imaging ($T_R = 1400$ ms; $T_E = 90$ ms) was used to acquire DW images (b-value = 1000 s/mm^2; 60 isotropically distributed gradient directions) from five axial slices (no gap; nominal voxel size $1.7 \times 1.7 \times 1.7$ mm^3; center slice aligned with slice from MT experiment). Seven data sets without diffusion weighting were recorded interleaved with the DW scans (initially and after each block of ten diffusion directions).

3.2. Analysis of Diffusion-Weighted Images

Pre-processing and tensor-based analysis of DW images was done using FSL 4.1.4 (`www.fmrib.ox.ac.uk/fsl`). A diffusion tensor was fitted to each voxel after corrections for eddy currents and B_0 inhomogeneities, and eigenvectors, eigenvalues, and the fractional anisotropy (FA) were extracted. Image regions outside the brain were excluded from the analysis of DW and MT data using a manually created binary mask. Voxels with FA < 0.3 were not considered to contain WM and were also excluded. A main fiber direction, θ_0, was retrieved from the angle between the principal eigenvector, $\boldsymbol{\epsilon}_1$, and $\mathbf{B}_0$ according to

$$\cos\theta_0 = (\boldsymbol{\epsilon}_1 \cdot \mathbf{B}_0) \,/\, (|\boldsymbol{\epsilon}_1| \; |\mathbf{B}_0|) \,. \tag{14}$$

Besides the simplifying diffusion tensor imaging (DTI) approach, scaled Bingham distributions were fitted to the fODF peaks to obtain a more specific characterization of the fiber configurations. For a full description of the procedures to estimate the five parameters in Eq. (12), we refer to Ref. [35]. In short, constrained spherical deconvolution, as implemented in MRtrix (`www.brain.org.au/software/mrtrix`), was applied to the DW data (after correction for T_2 weighting) [32], and the resulting fODF was approximated by eighth-order spherical harmonics expansion. A region in the corpus callosum was manually selected to compute the single fiber response function, which was used for the spherical deconvolution. Typically, the fODF comprises several peaks, which are assumed to reflect fiber bundles. For identifying these peaks, the fODF was overlayed with a discrete grid to search for local maxima. Bingham functions were fitted to the largest two maxima, whereas further peaks were considered to be artifacts

or noise in this analysis. In particular, direction vectors, $\boldsymbol{\mu}_1$ and $\boldsymbol{\mu}_2$, were fitted using an orientation matrix, and the concentration parameters, k_1 and k_2, were obtained by solving a system of linear equations.

3.3. Analysis of MT Images I: Standard MT Fitting

The procedures for BSB parameter fitting of MT data have been published in Ref. [17]. All algorithms were implemented in Matlab 8.1.0.604 (MathWorks, Natick, MA). Least-squares minimizations were performed using either Levenberg-Marquardt or trust-region-reflective algorithms; the latter one with and without parameter boundaries. We did not observe relevant differences in the results obtained by the different methods. All results reported subsequently were obtained with the trust-region-reflective method without setting boundaries.

Fits were based on calculations of the time evolution of the magnetization during the entire pulse sequence using matrix exponentials. Exact timing and shapes of all RF pulses were directly imported from the scanner and used in the calculations without simplifying assumptions. For better efficiency, polynomial interpolation was employed to calculate matrix exponentials without bias [17]. The B_0 and B_1 maps were used for pixel-by-pixel correction of offset frequencies and pulse amplitudes, respectively. To analyze the Z-spectra, all BSB parameters (including R_1^a) were directly fitted to the MT data acquired with different T_R [17]. R_1^b was always arbitrarily set to 1 s^{-1} [5].

As an initial analysis, the SL lineshape was calculated from Eq. (7) by numerical integration, and fitting was performed assuming $g^b = g^b_{\mathrm{SL}}$. This approach is subsequently referred to as "standard MT fitting". A sketch of the processing pipeline is indicated in Fig. 3a by the red pathway.

3.4. Analysis of MT Images II: MT Fitting Using the Novel Lineshape

For an alternative analysis, the novel RF absorption lineshape according to Eq. (13) was used instead of the SL (*i.e.*, $g^b = g^b_{\mathrm{fb}}$). This approach is subsequently referred to as "MT fitting with the fb lineshape". Except of the lineshape, there is no principle difference compared to "standard MT fitting". However, the approach is computationally more expensive because multiple integration steps, Eqs. (11) and (13), have to be performed for each voxel. Processing speed was enhanced by computing a lookup table with varying T_2^b for Eq. (11), from which all values required during fitting were obtained by cubic-spline interpolation. As a metric of the local fODF, Bingham parameters from fits to the DW images were used to generate individual maps of $\beta(\theta, \phi)$, and the values were

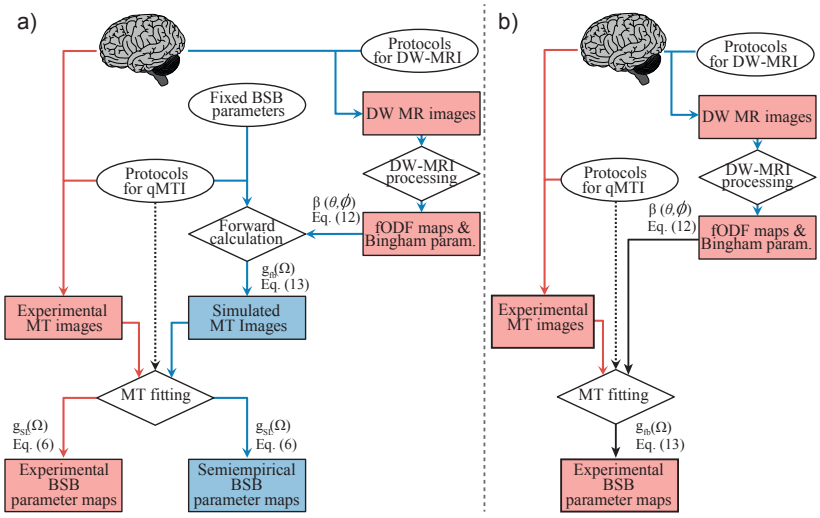

Figure 3: **(a)** Standard MT analysis of *in vivo* (red pathway) and simulated data (blue pathway). Experimental MT images are recorded with suitable protocols, and BSB parameter maps are fitted with an algorithm that reads the sequence data and assumes the SL lineshape. The same acquisition parameters and fixed BSB parameters are used to simulate MT images with the fiber-bundle lineshape, Eq. (13) and further input from parameterized experimental fODF maps. Subsequently, standard fitting with the SL lineshape yields semiempirical BSB parameter maps. **(b)** Equivalent steps used for MT fitting with the novel lineshape, where Eq. (13) is directly employed for fitting the MT data.

passed to the fitting procedure to compute g_{fb}^{b} from Eq. (13). A sketch of this processing pathway is shown in Fig. 3b.

3.5. Computer Simulations of qMTI

Semiempirical forward calculations of the magnetization's time evolution during MT experiments were performed with the aforementioned numerical methods to model Z-spectra for the same conditions (*i.e.*, with identical pulse shapes and sequence parameters) as employed in the *in-vivo* experiments. Typical BSB parameters for human WM summarized in Table 1 were assumed in the simulations, based on previous results [17, 39]. The tilde is used in Table 1 (and subsequently) to indicate *fixed* input parameters to forward calculations for better differentiation from *free* output parameters estimated by fitting (same symbols without tilde). Maps of all BSB parameters were calculated for all subjects comprising the following steps (blue pathway in Fig. 3a): *(i)* Generation of maps of $\beta(\theta, \phi)$. *(ii)* With the cylinder-model lineshape, Eq. (11), MT data were computed for the full range of potential single-axon orientations, $0° \leq \theta \leq 90°$. *(iii)* To consider multiple fiber orientations, the single-axon results were combined with the β maps as individual weighting factors according to Eq. (13). *(iv)* Standard MT fitting (with SL lineshape) to the simulated Z-spectra was performed to exactly mimic analysis type I of experimental data. The same input BSB parameters were used

for modeling all voxels in the segmented WM in all subjects. To further analyze the sensitivity to parameter variations, separate simulations were performed for different $\widetilde{T}_2^b$ values (range given in Table 1). This approach is subsequently referred to as "MT fitting of simulated data".

Table 1: Binary spin-bath model parameters used as input in the forward simulations.

$\widetilde{M_0^b/M_0^a}$	$\widetilde{R}_1^a$	$\widetilde{R}_1^b$	$\widetilde{T}_2^a$	$\widetilde{T}_2^b$	$\widetilde{RM_0^a}$	$\widetilde{R}_2^{\mathrm{res}}$
0.25	2.0 s^{-1}	1 s^{-1}	18 ms	12–15 μs	14 s^{-1}	31.4 s^{-1}

A similar approach was also used for an explorative evaluation of the novel lineshape, whereby Bingham parameters were chosen at will instead of being derived from DW data. Simulations were performed as above, but the fODF was calculated from a simplified version of Eq. (12) obtained by setting $k_1 = k_2 = \widetilde{k}$. A single fiber tract was assumed, and Z-spectra were calculated with the BSB parameters from Table 1 with variation of $\widetilde{T}_2^b$ and $\widetilde{k}$.

4. Results

4.1. Analyses Using Standard Methods

Typical parameter maps obtained with standard MT fitting are shown as Supplementary Figure S2. At this point, we focus on T_2^b for the analysis of orientation effects. Further T_2^b maps and corresponding main fiber orientations are shown in Fig. 4.

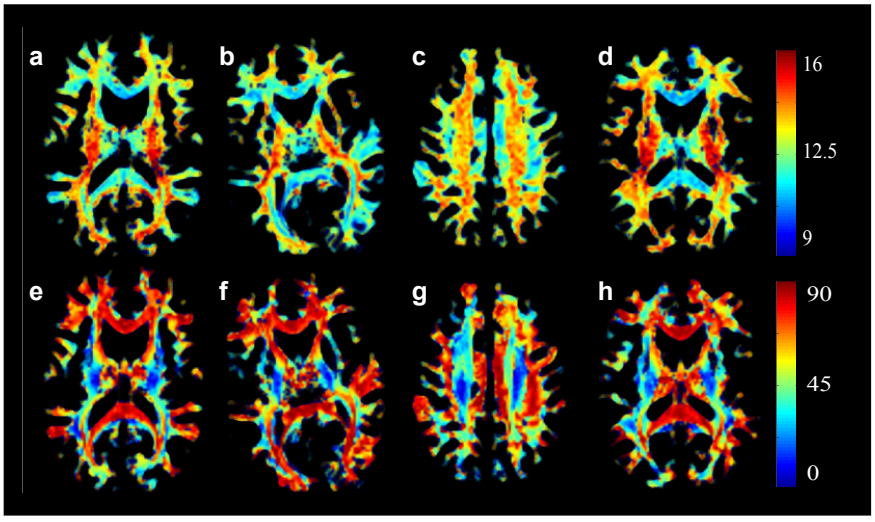

Figure 4: Color-coded parameter maps from cerebral WM in four healthy subjects. **(a–d)** T_2^b in μs, estimated by standard MT fits to the experimental data; **(e–h)** main fiber orientation in degrees obtained from the principal eigenvector of the diffusion tensor. Maps were interpolated from 128×96 to 256×192 for better visualization.

All slices are nearly perpendicular to $\mathbf{B}_0$. Thus, fibers running inferior–superior are parallel (blue on θ_0 maps), and those running anterior–posterior or left–right are orthogonal to $\mathbf{B}_0$ (red on θ_0 maps). A variation of T_2^b with orientation is clearly visible, and major fiber tracts can be identified on the T_2^b map. For example, T_2^b estimates are consistently smaller in the genu (gcc) and splenium (scc) of the corpus callosum (fibers approx. orthogonal to $\mathbf{B}_0$) than at positions where the corticospinal tract of the internal capsule (ic) penetrates the slice (fibers approx. parallel to $\mathbf{B}_0$). The cingulate gyrus part (cgc) and hippocampal part (cgh) of the cingulum can be separated from the gcc and the scc, respectively. In the more cranial slice (Fig. 4c), there is clear separation of the superior corona radiata (cr; mainly inferior–superior fibers, $\theta_0 \approx 10$–$40°$ and $T_2^b \approx 11$–12 μs) from the cgc (mainly anterior–posterior fibers, $\theta_0 \approx 70$–$90°$ and $T_2^b \approx 14$–16 μs).

The relation between T_2^b and θ_0 for the combined WM data (FA $\geq$ 0.3) from all subjects is shown in Fig. 5.

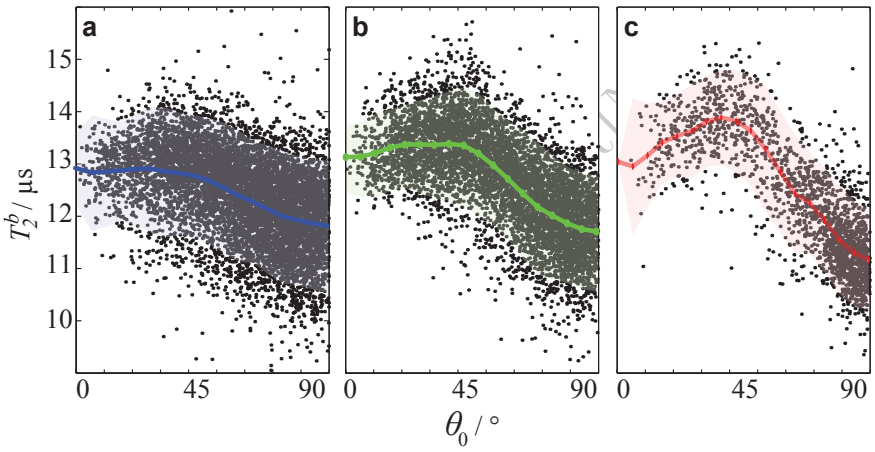

Figure 5: Plots of T_2^b (standard MT fits) in cerebral WM (experimental data from eight subjects) versus main fiber orientation (DTI results) for all voxels with **(a)** 0.3 < FA $\leq$ 0.5, **(b)** 0.5 < FA $\leq$ 0.7, and **(c)** FA > 0.7. Colored solid lines and shaded areas indicate the moving average ± one standard deviation (SD).

For better visualization of general features, the data were arbitrarily divided into three subsets differing by FA. For FA > 0.7, a peak with maximum $T_2^b \approx 14$ μs forms at orientations $\theta_0 \approx 30$–$50°$. Beyond this region, there are clear trends of decreasing T_2^b with both increasing θ_0 for $\theta_0 > 50°$ and decreasing θ_0 for $\theta_0 < 30°$. The same characteristics are also observed for FA < 0.7, however, they become more and more buried by increasing fluctuations in the estimates of T_2^b and/or θ_0.

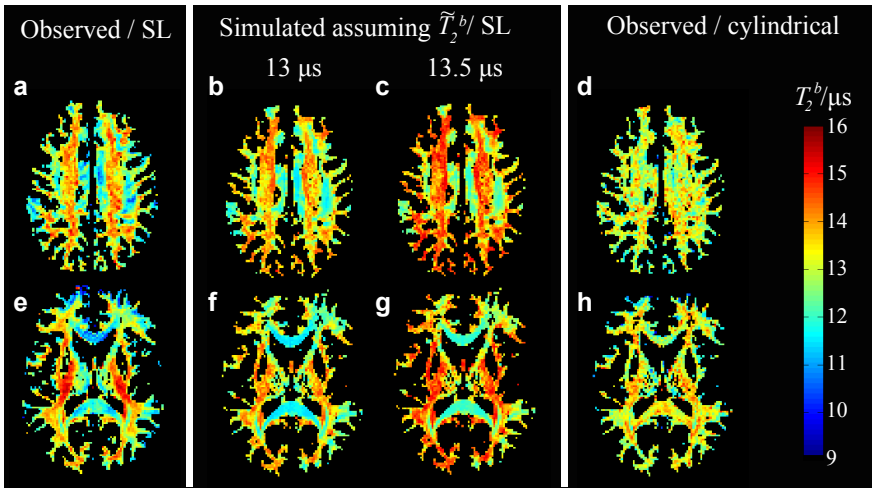

Figure 6: Color-coded experimental T_2^b maps obtained with standard MT fitting in two subjects **(a, e)** and results from semiempirical forward calculations with slightly different input parameters, $\widetilde{T}_2^b = 13$ μs **(b, f)** and 13.5 μs **(c, g)**. Excellent quantitative agreement with the experimental result is achieved with $\widetilde{T}_2^b = 13$ μs for subject 1 **(b)** and 13.5 μs for subject 2 **(f)**, whereas a subtle variation of $\widetilde{T}_2^b$ (in this case by 4 %) leads to a discernable offset. Also shown are results obtained by MT fitting using the novel lineshape (**d**, **h**).

4.2. Simulated MT Images

Results from standard MT fitting of simulated images (generated with Eq. (13) and experimental fODFs) are shown in Fig. 6.

Evidently, these fits using the SL lineshape yielded a spatial distribution of T_2^b although the same $\widetilde{T}_2^b$ had been used to simulate all voxels. The simulated maps show a high degree of correspondence with experimental T_2^b data from the same subject. The scaling of simulated T_2^b maps was sensitive to the input; that is, a subtle variation in $\widetilde{T}_2^b$ by 4% produced an appreciable deviation between simulated and experimental maps.

A comparison of experimental T_2^b as a function of the main fiber orientation and those obtained by forward simulations is shown in Fig. 7a. The influence obtained upon changing $\widetilde{T}_2^b$ from 13 μs to 13.5 μs (consistent with the maps in Figs. 6b, c, f, and g) is also shown.

As in Fig. 5c, a simple tensor analysis was used to estimate θ_0 from DW data, and only voxels with FA > 0.7 were included to highlight the general relations. Experimental and simulated data show excellent agreement for the full range of orientations. We emphasize that this match was achieved with identical fixed input values to the forward model for all voxels in all subjects.

The influence of a variation in the Bingham parameters on estimated $T_2^b(\theta_0)$ values is demonstrated in Fig. 8a.

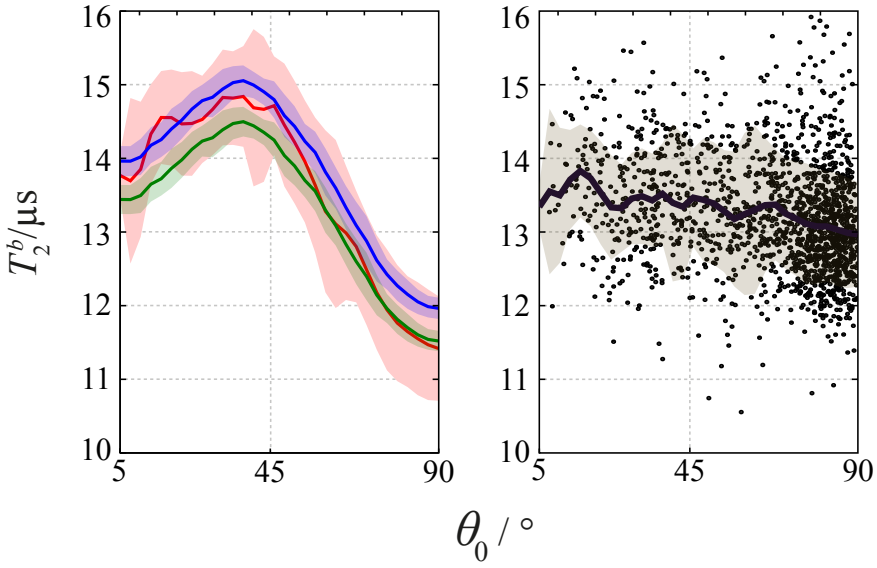

Figure 7: **(a)** Plots of T_2^b versus θ_0 comparing standard MT fits to experimental and simulated data (combined results from voxels with FA > 0.7 in all subjects). Solid lines and shaded areas indicate the moving average ± SD (red: experimental data; green and blue: simulations with $\widetilde{T}_2^b = 13$ μs and 13.5 μs, respectively). **(b)** Plots of T_2^b versus θ_0 (same voxels as in **(a)**) obtained by MT fitting using the novel lineshape. Solid lines and shaded areas indicate the moving average ± SD. Further individual plots of T_2^b versus θ_0 from all subjects are shown in Supplementary Figure S3.

Here, the main fiber orientation was taken from DW-MRI results assuming that each voxel contains only one fiber bundle, and the average concentration parameter, $\widetilde{k}$, was systematically varied. Results from standard MT fits to experimental data are also shown (identical data as in Fig. 7a). Simulations with $\widetilde{k} = 4.5$ and $\widetilde{T}_2^b = 13$ μs agreed well with the *in-vivo* data. With small values of $\widetilde{k}$, a distinct maximum of $T_2^b(\theta_0)$ is observed that flattens for larger $\widetilde{k}$ (Figs. 8a and b). As large values of $\widetilde{k}$ are equivalent to small FA values in the DTI approach, the flattened moving average of $T_2^b(\theta_0)$ observed experimentally with decreasing FA values (Fig. 5) is, therefore, reproduced by the simulations. As a further comparison, Fig. 8c demonstrates the influence from changing $\widetilde{T}_2^b$ with fixed $\widetilde{k} = 4.5$, which primarily produces a vertical shift of the curve.

In Fig. 9, all relevant BSB parameters obtained by standard MT fitting of the simulated data are compared, as a function of θ_0, to experimental results. The forward calculations yielded a rather subtle variation of all parameters with orientation, including M_0^b/M_0^a, R_1^a, T_2^a, and RM_0^a, which was, however, much less pronounced than the effect observed for T_2^b.

Except for T_2^b, such variations were smaller than experimental errors estimated in previous *in-vivo* studies [17] and, hence, negligible. Deviations from the simulations were observed experimentally for most BSB parameters (averaged data represented by solid

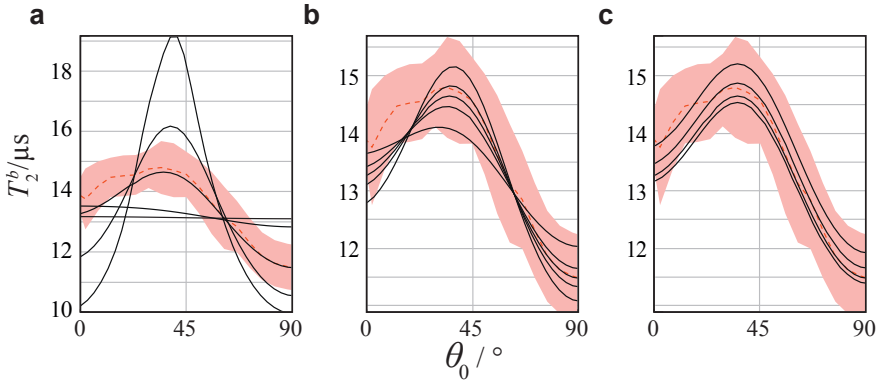

Figure 8: Plots of $T_2^b(\theta_0)$ obtained by standard MT fitting of simulated Z-spectra (black solid lines). with **(a)** $\widetilde{T}_2^b = 13$ μs and $\widetilde{k} = 0.1$, 1, 4.5, 10, and 100; **(b)** $\widetilde{T}_2^b = 13$ μs and $\widetilde{k} = 3$, 4, 4.5, 5, and 6; **(c)** $\widetilde{k} = 4.5$ and $\widetilde{T}_2^b = 12.9$, 13, 13.2, and 13.5 μs. Red broken lines and shaded areas indicate the *in-vivo* results from Fig. 5c. An increase in $\widetilde{k}$ primarily flattens the curve while an increase in $\widetilde{T}_2^b$ produces a shift.

lines in Fig. 9). This difference was minimal for T_2^b, whereas larger deviations occurred for M_0^b/M_0^a. Similarly, substantially increased variance was observed experimentally for constant θ_0, that is, when comparing voxels with similar main fiber orientation but from different brain locations and different subjects.

4.3. Analyses Using the Novel Lineshape

Results from fits of *in-vivo* data using the novel lineshape are shown in Figs. 6d and h. A spatial variation of T_2^b in relation to distinct fiber orientations is no longer evident in these maps. This is even more obvious in the flat moving average of $T_2^b(\theta_0)$ in Fig. 7b.

A comparison of all relevant BSB parameters obtained by MT fitting with the novel lineshape and with standard fitting is shown in Fig. 10 as a function of θ_0 (voxels with FA > 0.7). The distinct variation of T_2^b with θ_0 disappeared almost entirely when applying the novel lineshape, whereas the values for the other BSB parameters were quite similar for both methods.

5. Discussion

In the current work, we demonstrate an orientation dependence of MT in cerebral WM, namely of the associated transverse relaxation time T_2^b obtained with standard analysis. It can be explained by a fiber-bundle model that *(i)* adopts the BSB approach of two pools exchanging longitudinal magnetization; *(ii)* derives an absorption lineshape for the lipid components in myelin from dipolar interactions in liquid-crystalline membranes wrapped around a cylindrical axon segment; and *(iii)* utilizes an empirical fiber distribution obtained from DW-MRI. Simulations with the fiber-bundle lineshape reproduce

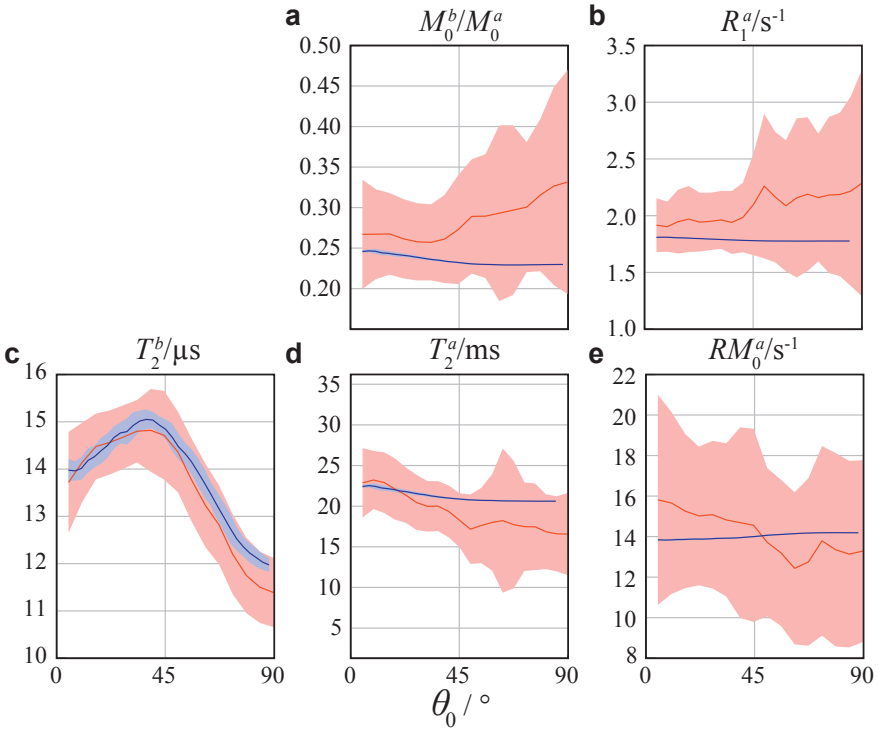

Figure 9: Plots of BSB parameters M_0^b/M_0^a **(a)**, T_1^a **(b)**, T_2^b **(c)**, T_2^a **(d)**, and RM_0^a **(e)**, in cerebral WM versus main fiber orientation (DTI results; only voxels with FA > 0.7). Solid lines and shaded areas indicate the moving average $\pm$ SD (combined data from all subjects) obtained by standard MT fits to the experimental (red) and simulated data (blue).

the effects observed *in vivo*.

Considering previous assumption that it is *"unlikely that MT anisotropy will be observed"* [10], we note that the orientation dependence found here is of apparent nature. In particular, it is the RF absorption by the semisolid pool that is anisotropic due to dipolar interactions in the partially ordered lipid bilayers of the myelin membrane. The orientation-dependent efficiency of saturation of the macromolecular resonance, in turn, modulates the cross-relaxation rate.

This variable efficiency can be modeled with the same $\widetilde{T}_2^b$ for different WM regions characterizing the average dipolar couplings in a lipid bilayer if additional information from the fODF is integrated. Most of the range of T_2^b values observed in normal WM with standard analysis is, thus, not due to a variation in such couplings (as it might result, *e.g.*, from changes in the membrane composition) but primarily reflects a residual angular term in the powder average of dipole-dipole interactions for a cylindrical arrangement of bilayers. This biophysical geometry is typical for myelin-containing WM, but not addressed when using the SL lineshape.

We note that our lineshape model ignores contributions from membranes that are

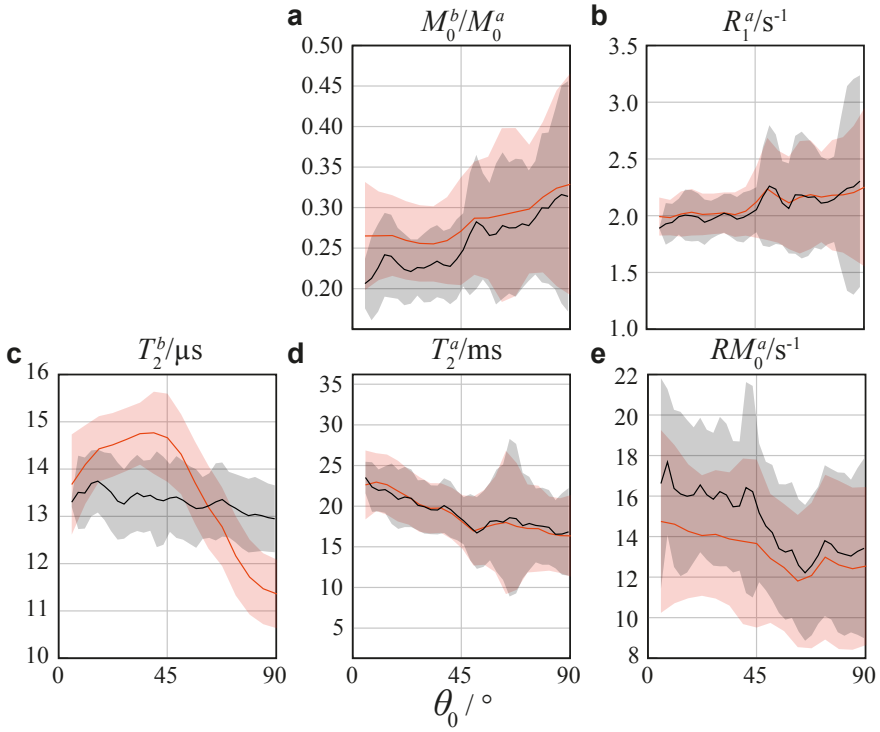

Figure 10: Plots of BSB parameters M_0^b/M_0^a **(a)**, T_1^a **(b)**, T_2^b **(c)**, T_2^a **(d)**, and RM_0^a **(e)**, in cerebral WM versus main fiber orientation (DTI results; only voxels with FA > 0.7). Solid lines and shaded areas indicate, respectively, the moving average ± SD (combined data from all subjects) obtained by fits using the standard SL lineshape (red) and the novel lineshape (black).

not arranged as cylinders (*e.g.*, from oligodendrocyte cell bodies or astrocytes). This seems to be justified as it is generally believed that myelin is the dominant source of MT in brain tissue [40–44]. 500pm-deep pockets in the water-lipid interface at cholesterol locations have been attributed a key role as interaction sites [40]. They are presumably filled with water forming relatively long-lived hydrogen bonds to hydroxyl groups of cholesterol and sphingomyelin [41, 43]. Alternatively, hydrogen bonds with galactose head groups of galactocerebrosides extending outward from the membrane have also been emphasized [44]. This view is based on careful experiments with artificial bilayers of different lipid composition [41–44]. Such studies are well suited to identify potential sources of efficient MT, however, they do not prove that the same effect is responsible for the contrast observed *in vivo* [44]. One difference is that the artificial systems lack proteins [40], which in myelin account for approximately 30% of the dry weight [45].

Although the fiber-bundle lineshape derived here is too non-specific to identify individual molecules, a common aspect with previous relaxation models is a reduction of the myelin membrane to its lipid constituents (as interaction sites). Previous work has shown that the dipolar broadened line of motionally constrained membrane proteins

(*e.g.*, myelin basic protein or proteolipid protein) is different from that of the liquid-crystalline lipid components [22, 46]. As the apparent T_2^b anisotropy observed *in vivo* is quantitatively explained by the new lineshape model without consideration of protein contributions, this might indicate that their contribution to MT is weak in cerebral WM. The hypothesis that cross-relaxation in WM can be adequately described by MT models that reduce the myelin membrane to its lipid constituents is also in agreement with studies of the origins of ultrashort T_2 signals by Horch *et al.* [47].

Although the fiber-bundle model achieves consistent simulations of orientation effects as observed *in vivo*, it is nevertheless a simplification. Cerebral WM is known to have multiple free water components with distinct values of T_2^a for axoplasmic and myelin water [48] and, at least at sufficiently high fields, correspondingly distinct values of T_1^a [49]. Hence, the reduction to a BSB does not correctly reflect the properties of all water pools in brain tissue [50, 51]. Moreover, the arrangement of membranes in the model (Fig. 1) is consistent with the structure of compact myelin but it does not account for the nodes of Ranvier and does not correctly describe the different morphology of the paranodal region flanking the nodes [52]. A potential role of these structures for MT is thus not addressed. However, the resulting pertubation may be expected to be small considering typical fractions occupied by the nodes and internodes along the length of an axon in the brain: Assuming 0.8 μm for the longitudinal extension of the node of Ranvier and 200-300 μm for the internode (data from rat optic nerve; [53]), the fraction occupied by paranodal regions is of the order of only 0.5%.

A substantial contribution to the increasing variance in the experimental results for FA < 0.7 (Fig. 5) is due to an inadequate definition of θ_0 by the simplifying DTI approach, especially for crossing fibers [28]. This could be improved by replacing $\boldsymbol{\epsilon}_1$ in Eq. (14) by $\boldsymbol{\mu}_0$ of the scaled Bingham distribution fitted to the largest fODF peak. However, even with a better definition of orientation, there will be some scatter due to variation in the fODF between voxels with the same θ_0. We note that this variance is addressed in our model in the term $\beta(\mathbf{u})$ in Eq. (13), which yields a corresponding variation in the voxel lineshape and, thereby, the scatter observed in the simulated data (Fig. 6).

In the forward simulations, all BSB parameters were fixed, primarily to reduce computation time. Despite this restriction, simulated and experimental T_2^b maps agreed well (Figs. 9c). While we might expect further improvement upon voxel-by-voxel adjustment

of the input parameters as achieved by fitting with the novel lineshape), a rather small variation of $\widetilde{T}_2^b$ (order of a few percent; Fig. 6) results from such adjustment. Hence, the apparent variation of T_2^b (Fig. 9c, red line) is almost entirely explained by orientation (blue line). This is different for other BSB parameters, in particular M_0^b/M_0^a. Here, no pronounced dependence on θ_0 is indicated by the forward simulations (Fig. 9a, blue line); that is, orientation effects do not explain the experimental result. For $\widetilde{T}_2^b$ (characterizing shape and width of the line), the narrow range is due to selective specificity to certain *types* of interaction sites facilitating efficient cross relaxation. $\widetilde{M_0^b/M_0^a}$ (*i.e.*, the line's amplitude), however, measures the *relative number* of such sites, and a larger range of values is required to match simulations and experimental results—consistent with previously observed correlations of MT parameters with myelination and fiber density [7, 54]. The result in Fig. 9a (blue solid line) further indicates that the estimation of M_0^b/M_0^a (unlike that of T_2^b) is relatively insensitive to orientation effects, that is, only minor errors are expected for standard BSB fitting without consideration of orientation). In our experiment, large values of M_0^b/M_0^a were observed particularly for major fiber tracts (*e.g.*, gcc, scc, or cgc). A similar conspicious appearance of main tracts on maps of the semisolid pool fraction has been previously reported by Yarnykh and Yuan [55] and, consistently, attributed to variations in the density of myelinated fibers.

The influence of WM fiber orientation on MR parameters, in particular, the effective transverse relaxation time, T_2^*, and phase contrast due to local B_0 inhomogeneity, has recently received substantial attention [56–60]. These observations can be explained by the tensorial (*i.e.*, anisotropic) characteristics of the magnetic susceptibility of myelin [61, 62]. Corresponding approaches to simulate magnitude and phase in GRE images bear remarkable similarities with our assumptions to characterize MT: *(i)* the myelin sheath is assumed to cause contrast behavior; *(ii)* it is represented as a hollow cylinder oriented at angle θ_0 to $\mathbf{B}_0$; *(iii)* its microstructure is modeled as wrapped bilayers of radially aligned lipids representing the source of anisotropy (*i.e.*, of magnetic susceptibility vs. dipolar line broadening in our case); *(iv)* membrane proteins are ignored. Quantitatively, however, anisotropic susceptibility causes frequency shifts of only a few Hz [56, 58, 59, 62], whereas the modulation of the dipolar lineshape with orientation is in the kHz range (Fig. 2).

An interesting aspect is finally, that our synthesis of the analysis of dipolar interaction leading to MT and a parameterization of anisotropic diffusion, that is, a combination

of fundamentally different contrast mechanisms (*i.e.*, cross relaxation vs. self diffusion) and imaging experiments (qMTI vs. DW-MRI) can also be exploited for evaluating DW-MRI techniques. A still persisting problem of tractography, and of DW-MRI in general, is the fact that no established gold standard is currently available for *in vivo* validation of the methodology in humans. In our forward simulations, an apparent orientation dependence of T_2^b was consistently produced with different assumptions of fiber distributions, such as a simple Gaussian distribution of orientations about a main direction (results not shown). However, the quantitative agreement with the experimentally observed change of T_2^b with θ_0 sensitively depended on the assumed distribution function. By far the best results (*i.e.*, almost perfect agreement; Fig. 9c) were achieved by modeling the fODF peaks as scaled Bingham distributions. This strongly supports the assumption that Eq. (12) yields a valid quantitative parametrization of the fiber population in a voxel.

6. Conclusion

Magnetization-transfer imaging in cerebral WM shows orientation dependence related to the cylindrical symmetry of liquid crystalline lipid bilayer membranes enveloping axons. This geometry gives rise to a distinct dipolar lineshape characterizing RF absorption by the semisolid proton pool. Forward simulations using the novel lineshape function along with information from the parametrized local fODF achieves excellent agreement with *in vivo* results in human brain. If orientation effects are appropriately addressed, $\widetilde{T}_2^b$ characterizing the inherent width of the absorption line shows very little variation between WM regions or among healthy young adults. Larger variation is observed for the relative size of the semisolid pool, which is thought to reflect the number of sites of efficient cross relaxation in the voxel, and is consistent with previous hypotheses relating M_0^b/M_0^a to myelination and/or fiber density of a fiber bundle. Consideration of orientation effects is relevant for a precise measurement of BSB parameters, in particular T_2^b. In comparison, estimates of M_0^b/M_0^a are more robust, and standard qMTI analysis with the isotropic SL lineshape is expected to yield meaningful results. The excellent agreement between orientation effects observed in qMTI and maps computed using experimental DW-MRI results as input further indicates that the scaled Bingham distribution is a valid parametrization of the fODF peaks.

Acknowledgments

We thank Thies Jochimsen for support with ODIN (`od1n.sourceforge.net`). This work was funded in part by the Helmholtz Alliance "ICEMED–Imaging and Curing Environmental Metabolic Diseases". Creation of Fig. 1 employed the `SpinDynamica` code for `Mathematica`, programmed by Malcolm H. Levitt, with contributions from J. Rantaharju, A. Brinkmann, and S. S. Roy, available at `www.SpinDynamica.soton.ac.uk`.

References

[1] R.G. Bryant and J.-P. Korb. Nuclear magnetic resonance and spin relaxation in biological systems. *Magn. Reson. Imaging*, 23(2):167–173, 2005.

[2] H.T. Edzes and E.T. Samulski. Cross relaxation and spin diffusion in proton NMR of hydrated collagen. *Nature*, 265(5594):521–523, 1977.

[3] S.D. Wolff and R.S. Balaban. Magnetization transfer contrast (MTC) and tissue water proton relaxation *in vivo*. *Magn. Reson. Med.*, 10(1):135–144, 1989.

[4] J. Grad and R.G. Bryant. Nuclear magnetic cross-relaxation spectroscopy. *J. Magn. Reson.*, 90(1):1–8, 1990.

[5] R.M. Henkelman, X.M. Huang, Q.S. Xiang, G.J. Stanisz, S.D. Swansosn, and M.J. Bronskill. Quantitative interpretation of magnetization transfer. *Magn. Reson. Med.*, 29(6):759–766, 1993.

[6] C. Laule, I.M. Vavasour, S.H. Kolind, D.K.B. Li, T.L. Traboulsee, G.R.W. Moore, and A.L. MacKay. Magnetic resonance imaging of myelin. *Neurotherapeutics*, 4(3):460–484, 2007.

[7] K. Schmierer, D.J. Tozer, F. Scaravilli, D.R. Altmann, G.J. Barker, P.S. Tofts, and D.H. Miller. Quantitative magnetization transfer imaging in postmortem multiple sclerosis brain. *J. Magn. Reson. Imaging*, 26(1):41–51, 2007.

[8] F. Volke, S. Eisenblätter, J. Galle, and G. Klose. Dynamic properties of water at phosphatidylcholine lipid bilayer surfaces as seen by deuterium and pulsed field gradient proton NMR. *Chem. Phys. Lipids*, 70:121–131, 1994.

[9] K.E. Chappell, M.D. Robson, A. Stonebridge-Foster, A. Glover, J.M. Allsop, A.D. Williams, A.H. Herlihy, J. Moss, P. Gishen, and G.M. Bydder. Magic angle effects in MR neurography. *AJNR Am. J. Neuroradiol.*, 25(3):431–440, 2004.

[10] R.M. Henkelman, G.J. Stanisz, J.K. Kim, and M.J. Bronskill. Anisotropy of NMR properties of tissues. *Magn. Reson. Med.*, 32(5):592–601, 1994.

[11] D. Müller, A. Pampel, and H.E. Möller. Orientation dependence of magnetization transfer in human white matter. *Proc. Intl. Soc. Mag. Reson. Med.*, 18:2996, 2010.

[12] V.L. Yarnykh. Fast macromolecular proton fraction mapping from a single off-resonance magnetization transfer measurement. *Magn. Reson. Med.*, 68(1):166–178, 2012.

[13] H. Wennerström. Proton nuclear magnetic resonance lineshapes in lamellar liquid crystals. *Chem. Phys. Lett.*, 18(1):41–44, 1973.

[14] C. Morrison and R.M. Henkelman. A model for magnetization transfer in tissues. *Magn. Reson. Med.*, 33(4):475–482, 1995.

[15] C. Morrison, G. Stanisz, and R.M. Henkelman. Modeling magnetization transfer for biological-like systems using a semi-solid pool with a super-Lorentzian lineshape and dipolar reservoir. *J. Magn. Reson. B*, 108(2):103–113, 1995.

[16] J.G. Sled and G.B. Pike. Quantitative interpretation of magnetization transfer in spoiled gradient echo MRI sequences. *J. Magn. Reson.*, 145(1):24–36, 2000.

[17] D.K. Müller, A. Pampel, and H.E. Möller. Matrix-algebra-based calculations of the time evolution of the binary spin-bath model for magnetization transfer. *J. Magn. Reson.*, 230:88–97, 2013.

[18] H.M. McConnell. Reaction rates by nuclear magnetic resonance. *J. Chem. Phys.*, 28(3):430–431, 1958.

[19] S.J. Graham and R.M. Henkelman. Understanding pulsed magnetization transfer. *J. Magn. Reson. Imaging*, 7(5):903–912, 1997.

[20] M. Bloom, E.E. Burnell, A.L. MacKay, C.P. Nichol, M.I. Valic, and G. Weeks. Fatty acyl chain order in lecithin model membranes determined from proton magnetic resonance. *Biochemistry*, 17(26):5750–5762, 1978.

[21] M. Bloom, E.E. Burnell, S.B.W. Roeder, and M.I. Valic. Nuclear magnetic resonance line-shapes in lyotropic liquid-crystals and related systems. *J. Chem. Phys.*, 66(7):3012–3020, 1977.

[22] A.L. MacKay. A proton NMR moment study of the gel and liquid-crystalline phases of dipalmitoyl phosphatidylcholine. *Biophys. J.*, 35:301–313, 1981.

[23] G. Lindblom and G. Orädd. NMR studies of translational diffusion in lyotropic liquid crystals and lipid membranes. *Prog. Nucl. Magn. Reson. Spectrosc.*, 26:483–515, 1994.

[24] F. Volke and A. Pampel. Membrane hydration and structure on a subnanometer scale as seen by high resolution solid state nuclear magnetic resonance: POPC and POPC/C12E04 model membranes. *Biophys. J.*, 68(5):1960–1965, 1995.

[25] J. H. Davis, M. Auger, and R.S. Hodges. High resolution 1H nuclear magnetic resonance of a transmembrane peptide. *Biophys. J.*, 69(5):1917–1932, 1995.

[26] C. Glaubitz and A. Watts. Magic angle-oriented sample spinning (MAOSS): A new approach toward biomembrane studies. *J. Magn. Reson.*, 130(2):305–316, 1998.

[27] A. Abragam. *The Principles of Nuclear Magnetism*. International Series of Monographs on Physics. Clarendon Press, Oxford, 1961.

[28] D.K. Jones, T.R. Knösche, and R. Turner. White matter integrity, fiber count, and other fallacies: The do's and don'ts of diffusion MRI. *NeuroImage*, 73(1):239–254, 2013.

[29] T.B. Leergaard, N.S. White, A. de Crespigny, I. Bolstad, H. D'Arceuil, J.G. Bjaalie, and A.M. Dale. Quantitative histological validation of diffusion MRI fiber orientation distributions in the rat brain. *PloS ONE*, 5(1):e8595, 2010.

[30] A.S. Choe, I. Stepniewska, D.C. Colvin, Z. Ding, and A.W. Anderson. Validation of diffusion tensor MRI in the central nervous system using light microscopy: Quantitative comparison of fiber properties. *NMR Biomed.*, 25(7):900–908, 2012.

[31] I. Ronen, M. Budde, E. Ercan, J. Annese, A. Techawiboonwong, and A. Webb. Microstructural organization of axons in the human corpus callosum quantified by diffusion-weighted magnetic resonance spectroscopy of *N*-acetylaspartate and post-mortem histology. *Brain Struct. Funct.*, 219(5):1773–1785, 2014.

[32] J.D. Tournier, F. Calamante, and A. Connelly. Robust determination of the fibre orientation distribution in diffusion MRI: Non-negativity constrained super-resolved spherical deconvolution. *NeuroImage*, 35(4):1459–1472, 2007.

[33] E. Kaden, T.R. Knösche, and A. Anwander. Parametric spherical deconvolution: Inferring anatomical connectivity using diffusion MR imaging. *NeuroImage*, 37(2):474–488, 2007.

[34] K.K. Seunarine, P.A. Cook, M.G. Hall, K.V. Embleton, G.J.M. Parker, and D.C. Alexander. Exploiting peak anisotropy for tracking through complex structures. In *IEEE 11th International Conference on Computer Vision*, pages 2649–2656, 2007.

[35] T.W. Riffert, J. Schreiber, A. Anwander, and T.R. Knösche. Beyond fractional anisotropy: Extraction of bundle-specific structural metrics from crossing fiber models. *NeuroImage*, 100:176–191, 2014.

[36] C. Bingham. Antipodally symmetric distribution on sphere. *Ann. Stat.*, 2(6):1201–1225, 1974.

[37] V.J. Schmithorst, B.J. Dardzinski, and S.K. Holland. Simultaneous correction of ghost and geometric distortion artifacts in EPI using a multiecho reference scan. *IEEE Trans. Med. Imaging*, 20(6):535–539, 2001.

[38] V.L. Yarnykh. Actual flip-angle imaging in the pulsed steady state: A method for rapid three-dimensional mapping of the transmitted radiofrequency field. *Magn. Reson. Med.*, 57(1):192–200, 2007.

[39] J.G. Sled and G.B. Pike. Quantitative imaging of magnetization transfer exchange and relaxation properties in vivo using MRI. *Magn. Reson. Med.*, 46(5):923–931, 2001.

[40] S.H. Koenig, R.D. Brown, III, M. Spiller, and N. Lundblom. Relaxometry of brain: Why white matter appears bright in MRI. *Magn. Reson. Med.*, 14(3):482–495, 1990.

[41] S.H Koenig. Cholesterol of myelin is the determinant of gray-white contrast in MRI of brain. *Magn. Reson. Med.*, 20(2):285–291, 1991.

[42] T.A. Fralix, T.L. Ceckler, S.D. Wolff, S.A. Simon, and R.S. Balaban. Lipid bilayer and water proton magnetization transfer: Effect of cholesterol. *Magn. Reson. Med.*, 18(1):214–223, 1991.

[43] T.L. Ceckler, S.D. Wolff, V. Yip, S.A. Simon, and R.S. Balaban. Dynamic and chemical factors affecting water proton relaxation by macromolecules. *J. Magn. Reson.*, 93(3):637–645, 1992.

[44] W. Kucharczyk, P.M. Macdonald, G.J. Stanisz, and R.M. Henkelman. Relaxivity and magnetization transfer of white matter lipids at MR imaging: Importance of cerebrosides and pH. *Radiology*, 192(2):521–529, 1994.

[45] O. Jahn, Tenzer S., and H.B. Werner. Myelin proteomics: Molecular anatomy of an insulating sheath. *Mol. Neurobiol.*, 40(1):55–72, 2009.

[46] M. Bloom, K.T. Holmes, C.E. Mountford, and P.G. Williams. Complete proton magnetic resonance in whole cells. *J. Magn. Reson.*, 69(1):73–81, 1986.

[47] R. A. Horch, J. C. Gore, and M. D. Does. Origins of the ultrashort-T_2 ^{1}H NMR signals in myelinated nerve: A direct measure of myelin content? *Magn. Reson. Med.*, 66(1):24–31, 2011.

[48] A. MacKay, K. Whittall, J. Adler, D. Li, D. Paty, and D. Graeb. *In vivo* visualization of myelin water in brain by magnetic resonance. *Magn. Reson. Med.*, 31(2):673–677, 1994.

[49] C. Labadie, J.H. Lee, W.D. Rooney, S. Jarchow, M. Aubert-Frécon, C.S. Springer, Jr., and H.E. Möller. Myelin water mapping by spatially regularized longitudinal relaxographic imaging at high magnetic fields. *Magn. Reson. Med.*, 71(1):375–387, 2014.

[50] G.J. Stanisz, A. Kecojevic, M.J. Bronskill, and R.M. Henkelman. Characterizing white matter with magnetization transfer and T_2. *Magn. Reson. Med.*, 42(6):1128–1136, 1999.

[51] A. MacKay, C. Laule, I. Vavasour, S. Kolind, and B. Mädler. Insights into brain microstructure from the T_2 distribution. *Magn. Reson. Imaging*, 24(4):515–525, 2006.

[52] N. Baumann and D. Pham-Dinh. Biology of oligodendrocyte and myelin in the mammalian central nervous system. *Physiol. Rev.*, 81(2):871–927, 2001.

[53] S.G. Waxman, J.D. Kocsis, and P.K. Stys, editors. *The Axon: Structure, Function and Pathophysiology*. Oxford University Press, New York, 1995.

[54] K. Schmierer, F. Scaravilli, D.R. Altmann, G.J. Barker, and D.H. Miller. Magnetization transfer ratio and myelin in postmortem multiple sclerosis brain. *Ann. Neurol.*, 56(3):407–415, 2004.

[55] V.L. Yarnykh and C. Yuan. Cross-relaxation imaging reveals detailed anatomy of white matter fiber tracts in the human brain. *NeuroImage*, 23(1):409–424, 2004.

[56] X. He and D.A. Yablonskiy. Biophysical mechanisms of phase contrast in gradient echo MRI. *Proc. Natl. Acad. Sci. USA*, 106(32):13558–13563, 2009.

[57] B. Bender and U. Klose. The in vivo influence of white matter fiber orientation towards B_0 on T2* in the human brain. *NMR Biomed.*, 23(9):1071–1076, 2010.

[58] J. Lee, K. Schmueli, M. Fukunaga, P. van Gelderen, H. Merkle, A.C. Silva, and J.H. Duyn. Sensitivity of MRI resonance frequency to the orientation of brain tissue microstructure. *Proc. Natl. Acad. Sci. USA*, 107(11):5130–5135, 2010.

[59] C. Liu. Susceptibility tensor imaging. *Magn. Reson. Med.*, 63(6):1471–1477, 2010.

[60] C. Denk, E.H. Torres, A. MacKay, and A. Rauscher. The influence of white matter fibre orientation on MR signal phase and decay. *NMR Biomed.*, 24(3):246–252, 2011.

[61] W. Li, B. Wu, A.V. Avram, and C. Liu. Magnetic susceptibility anisotropy of human brain *in vivo* and its molecular underpinnings. *NeuroImage*, 59:2088–2097, 2012.

[62] S. Wharton and R. Bowtell. Fiber orientation-dependent white matter contrast in gradient echo MRI. *Procs. Natl. Acad. Sci. USA*, 109(45):18559–18564, 2012.

Supplementary Material

Apparent Orientation Dependence of Magnetization Transfer Parameters in Human White Matter

André Pampel, Dirk K. Müller, Alfred Anwander, Henrik Marschner, Harald E. Möller

Max Planck Institute for Human Cognitive and Brain Sciences, Stephanstr. 1a, 04103 Leipzig, Germany

Abbreviations:
BSB = binary spin bath; cgc = cingulum cingulate gyrus part; cgh = cingulum hippocampal part; cr = corona radiata; cyl = cylinder; DTI = diffusion tensor imaging; DW = diffusion weighted; FA = fractional anisotropy; fODF = fiber orientation distribution function; FOV = field of view; gcc = genu of corpus callosum; GRE = gradient-recalled echo; MRI = magnetic resonance imaging; MT = magnetization transfer; NMR = nuclear magnetic resonance; qMTI = quantitative magnetization-transfer imaging; RF = radiofrequency; scc = splenium of corpus callosum; SD = standard deviation; SL = super-Lorentzian; WM = white matter.

Mathematical symbols:

$_a$, $_b$:	indices for the liquid and semisolid proton pools
$\tilde{}$:	indicates a fixed parameter
$\mathbf{B}_0$:	static magnetic field
B_0:	static magnetic field amplitude
B_1:	RF field amplitude
b:	b-value
f:	frequency distribution
f_0:	scaling factor in the Bingham distribution
g;	absorption lineshape function
g_{fb}:	fiber-bundle lineshape function (cylinder-Bingham model)
g_{SL}:	super-Lorentzian lineshape function
g_{cyl}:	single-fiber lineshape function (cylinder model)
$\hat{\mathcal{H}}_D$:	dipolar Hamiltonian
$\langle\hat{\mathcal{H}}_D(0)\rangle$:	isotropic part of the time-averaged dipolar Hamiltonian
i:	integer
$\widetilde{k}$:	average concentration parameter in the Bingham distribution
k_1, k_2:	concentration parameters in the Bingham distribution
M_0:	equilibrium magnetization
M_z:	longitudinal magnetization component
$\mathcal{N}$:	normalization constant
P_2	second Legendre polynomial
R:	MT rate constant
R_1:	longitudinal relaxation rate constant

R_1^{obs}:	observed longitudinal relaxation rate constant
R_2:	transverse relaxation rate constant
R_2^{res}:	residual relaxation rate
R_2^{tot}:	total relaxation rate
R_{rf}^b:	saturation rate constant of the semisolid pool
r_2^b:	orientation-dependent relaxation rate
T_1:	longitudinal relaxation time
T_2:	transverse relaxation time
T_2^*:	effective transverse relaxation time
T_E:	echo time
T_I:	inversion time
T_R:	repetition time
$\mathbf{u}$:	point on the surface of the unit sphere
x, y, z:	Cartesian coordinates in the laboratory frame
x_A, y_A, z_A:	Cartesian coordinates in the axon frame
α	RF pulse flip angle
α_{sat}	nominal on-resonance saturation pulse flip angle
β:	scaled Bingham distribution
γ:	magnetogyric ratio
$\boldsymbol{\epsilon}_1$:	principal eigenvector of the diffusion tensor
θ:	polar angle (of axon axis) in the laboratory frame
θ_0:	main fiber orientation
θ_n:	polar angle between membrane normal and $\mathbf{B}_0$
$\boldsymbol{\mu}_0$:	direction of the mean of the Bingham distribution
$\boldsymbol{\mu}_1$, $\boldsymbol{\mu}_2$:	directions in the Bingham distribution
σ:	scaling factor
ϕ:	azimuth in the laboratory frame
ϕ_A:	azimuth in the axon frame
Ω:	offset frequency in rad/s
ω_0:	Larmor frequency in rad/s
ω_1:	RF field amplitude in rad/s
$\omega_{1,max}$:	maximum ω_1 value of amplitude-modulated RF pulse
ω_{rf}:	frequency of the RF field in rad/s

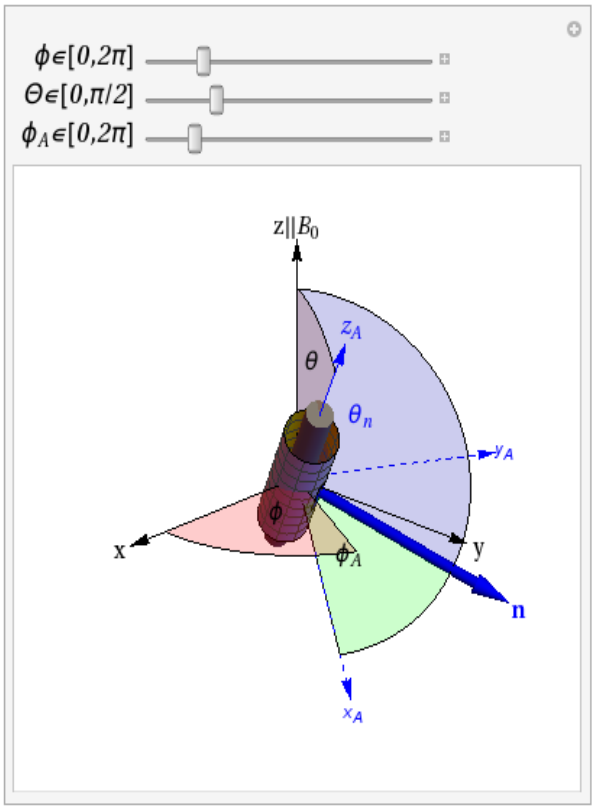

Supplementary Figure S1: Spherical coordinates describing the orientation of a bilayer segment wrapped around a cylindrical axon. The polar angle of the membrane normal in the laboratory frame, xyz, is θ_n. Transformation into an axon frame, $x_A y_A z_A$, for which the z_A-axis is defined by the cylinder axis, is achieved by subsequent rotations about the y-axis by θ, and about the z-axis by ϕ. The azimuth of the membrane normal in the axon frame is ϕ_A. Note that θ_n does not depend on ϕ.

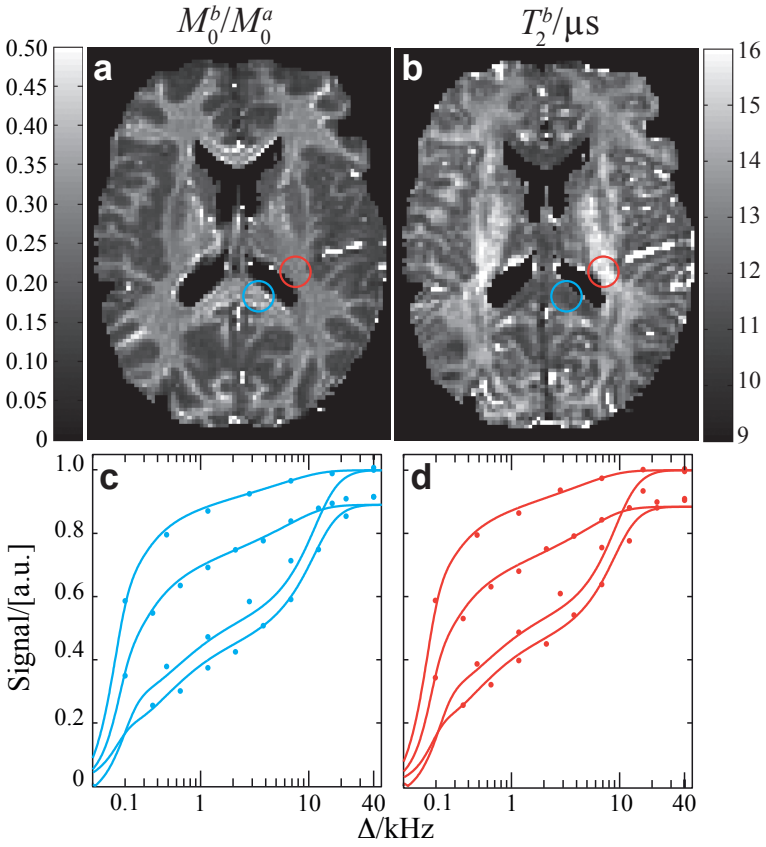

Supplementary Figure S2: Examples of experimental maps of the BSB parameters M_0^b/M_0^a **(a)** and T_2^b **(b)** from one subject as well as corresponding Z-spectra (red and blue symbols) and results from standard fitting with the SL lineshape (red and blue solid lines) in two selected pixels in the splenium of the corpus callosum **(c)** and the internal capsule **(d)**. The positions of the selected pixels are in the center of the red and blue circle, respectively. Only a subset of the experimental data points recorded at $T_R = 33.6$ and 80 ms are displayed in the Z-spectra to avoid excessive overlap of the fitted curves; $\Delta = \Omega/(2\pi)$.

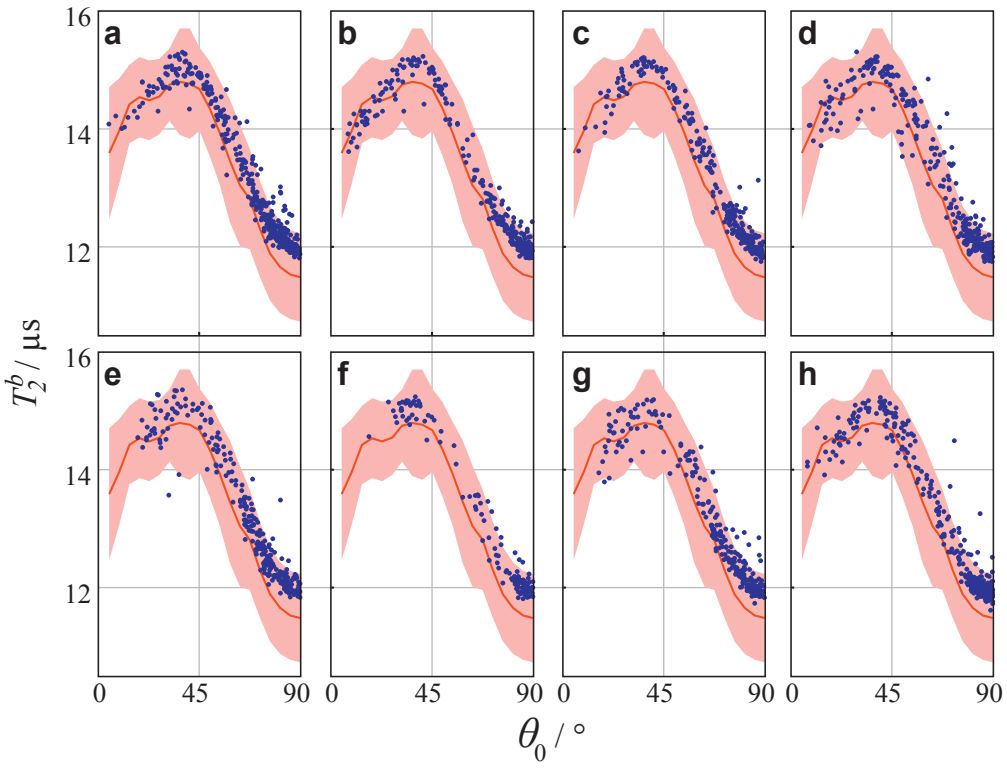

Supplementary Figure S3: Plots of T_2^b versus θ_0 comparing standard fits to experimental and simulated data (voxels with FA > 0.7) for all subjects. ed solid lines and shaded areas indicate the moving average $\pm$ SD of experimental T_2^b and blue filled circles show simulations for the same voxels. Identical BSB parameters (Table 1) with $\widetilde{T}_2^b = 13.5$ μs) were used in all simulations.